RSC Advances

ROYAL SOCIETY OF CHEMISTRY

www.rsc.org/advances

Preparation and microwave absorption properties of multi-walled carbon nanotubes decorated with Ni-doped SnO_2 nanocrystal

Ling Lin, Honglong Xing,* Ruiwen Shu, Lei Wang , Xiaoli Ji ,Dexin Tan and Ying Gan

School of Chemical Engineering, Anhui University of Science and Technology, Huainan 232001, China

*Corresponding authors:

Tel: (86)-554-6668497

E-mail: austxhl@163.com

In this work, Ni-doped SnO_2@MWCNTs composites were synthesized by a facile one-step hydrothermal method. The morphology and structure of the as-prepared composites were characterized by XRD, SEM, TEM, XPS, FT-IR and Raman. It was found that SnO_2 nanoparticles were successfully anchored on the MWCNTs with a diameter of 3-5 nm and the Ni^{2+} had successfully doped into SnO_2@MWCNTs. Moreover, the effect of doped Ni molar percentage on the electromagnetic parameters and microwave absorbing properties of the Ni-doped SnO_2@MWCNTs composites were studied in the 2-18 GHz frequency range. The results showed that the composites with 28.2% doped Ni content exhibited the best microwave absorbing properties. The maximum *RL* reached -39.2 dB at 8.2 GHz with a thickness of 2.5 mm, and the bandwidth of *RL* lower than -10 dB was 3.6 GHz (from 12.6 to 16.2 GHz) with a thickness of 1.5 mm. The excellent microwave absorbing properties could be attribute to the good impedance match, Debye relaxation, interfacial polarization and the high conductivity of MWCNTs component. It was believed that the Ni-doped SnO_2@MWCNTs composites could be used as a new type of microwave absorbing materials against electromagnetic pollution.

1. Introduction

Microwave absorbing materials have attracted much attention due to the increasingly electromagnetic (EM) pollution problems, which not only influence the performance of electronic devices, but also be harmful to the health of human beings. [1, 2] Carbon nanomaterials, especially multi-walled carbon nanotubes (MWCNTs) have attracted significant interest in microwave absorption field due to their excellent physicochemical properties, such as good chemical stability, lightweight, high electrical conductivity, low cost and unique one dimensional tubular structure.[3,4,5,6]

In order to meet the requirements of new type microwave absorption materials, such as thin thickness, light weight, wide absorption frequency band and strong absorption, it is necessary to decorate or fill in/on MWCNTs to improve microwave attenuation capacity.[3,7,8,9,10,11]For example, Lu *et al*. reported that MWCNTs decorated with ZnO nanocrystals had highly efficient microwave absorption properties at elevated temperature.[3] Wang *et al*. fabricated MWCNT/CdS nanocomposites via a one-step chemical co-precipitation approach and found that the composites exhibited excellent microwave absorbing properties, i.e. the maximum reflection loss (*RL*) reached -45 dB with a thickness of 1.5 mm and the absorption bandwidth of *RL* lower than -15 dB was 2.4 GHz.[11] Tin oxide (SnO_2) is one of the most important n-type semiconductor materials with a wide band gap of 3.6 eV at room temperature.[12] It has many unique properties such as high optical transparency, electrical conductivity and chemical sensitivity, which made it become an attractive material for application in dye-Sensitized solar cells, [13] field effect transistors, [14] catalysis [15, 16] and gas-sensing[17,18]. In recent years, SnO_2 has attracted significant attention due to its remarkable microwave absorption properties.[19,20,21] As is well known, the microwave

absorption performance can be determined by the complex permeability/permittivity and EM impedance matching. For the MWCNTs/semiconductor nanocomposites, the lack of permeability lead to the poor EM impedance matching, indicating that the desired EM absorption performance can not be reached in the present system.

Magnetic metal doping is an effective way to solve this problem. Compared with Fe and Co, Ni possesses the higher relative permeability and good anti-oxidation performance, leading to that Ni have better magnetic loss and be widely used as the microwave absorbers. Nickel has been extensively used in the field of microwave absorption, owing to its easy preparation and low cost.[22,23] However, Ni would induce an eddy current by microwave in the GHz range because of its high electrical conductivity. To alleviate this problem, an effective way is to prepare complex structures of Ni or synthesize Ni-based composites, such as Ni@Al_2O_3, Ni@TiO_2 core-shell particles, Ni-ZnO and so on, which have been synthesized and their EM performances have been investigated in detail.[12,22,23]

Based on our other work (submitted to other Journal), we synthesized magnetic metal (Fe, Co, Ni) doped ZnO/Al composites, and discussed the microwave absorption of the composites. The results showed that Ni ions doping ZnO/Al composites have the best microwave absorption.

In addition, due to the nearly equal ionic radii of Ni^{2+} ions (0.69 Å) and Sn^{4+} ions (0.71 Å),[24] Ni ions can effectively substituted Sn ions. Therefore, the synthesis of Ni-doped SnO_2/MWCNTs is imperative if it is to be used as the microwave absorber. However, to the best of our knowledge, there are no references on the microwave absorption properties of magnetic metal ion such as Ni-doped SnO_2@MWCNTs composites has been reported so far.

In the present study, the Ni-doped SnO_2@MWCNTs composites were prepared

by a facile one-step hydrothermal method. The structure, morphology and interfacial interactions between Ni-doped SnO_2 and MWCNTs were explored. Moreover, the effect of doped Ni molar percentage on the electromagnetic parameters and microwave absorbing properties of the Ni-doped SnO_2@MWCNTs composites were investigated. The resulting composites is promising and lightweight for a practical use of electromagnetic wave absorption applications in the areas of stealth technology.

2 Experimental Section

2.1 Materials

MWCNTs of 5-15 nm in diameter and 10-20 μm in length were provided by Chengdu Organic Chemcials Co. Ltd. HNO_3 solution (65 wt%), HCl solution (38 wt%), ammonia solution (25 wt%), $SnCl_4 \cdot 5H_2O$ and $Ni(NO_3)_2 \cdot 6H_2O$ were purchased from Sinopharm Chemical Reagent Co. Ltd. All the chemical reagents were analytical grade and were used without further purification. Water was purified by deionization and filtration with a Millipore purification apparatus (18.2 MΩ·cm).

2.2 Modification of MWCNTs

MWCNTs were treated by refluxing in 65 wt% HNO_3 at 120 ^oC for 6 h to prepare functionalized MWCNTs. The acid-treated MWCNTs were washed several times with deionized water until pH became neutral and then dried in a vacuum oven at 60 ^oC for 24 h.

2.3 Preparation of Ni-doped SnO_2@MWCNTs composites

The Ni-doped SnO_2@MWCNTs composites were prepared via a facile hydrothermal

method. Typically, the acid-treated MWCNTs (0.04 g) was firstly dispersed in 40 mL of deionized water by ultrasonication for 2 h. Then, HCl (38%, 0.7 mL), $SnCl_4 \cdot 5H_2O$ (1.55 g) and $Ni(NO_3)_2 \cdot 6H_2O$ with different Ni^{2+} molar percentage against ($Ni^{2+} + Sn^{4+}$) (0%, 5.5%, 10.7%, 20.0%, 28.2%, and 35.4%) were added into the above aqueous dispersion of MWCNTs under magnetic stirring until completely dissolved. Next, $NH_3 \cdot H_2O$ (25 wt%) was added drop-wise into the reaction mixture to adjust the pH equal to 9. After that, the reaction mixture was transferred into a 100 mL Teflon-lined stainless steel autoclave and reacted at 160 °C for 18 h. Lastly, the resulting products were separated by centrifuging and washed with ethanol and de-ionized water several times until pH became neutral and then dried in a vacuum oven at 55 °C for 24 h. For comparison, the SnO_2@MWCNTs composites were also prepared by similar hydrothermal procedures without adding $Ni(NO_3)_2 \cdot 6H_2O$.

2.4 Materials characterization

The crystalline structure of the synthesized samples were characterized by X-ray diffraction (XRD) using a LabX XRD-6000 (Shimadzu, Japan) with Cu-Kα radiation (λ = 0.154 nm) in the scattering range (2θ) of 10-80^o with a scan rate of 2 ^{o}/min. The Raman spectra were acquired at room temperature using LabRAM-HR (Horiba Jobin Yvon, France) over the range of 500-3400 cm^{-1}. The Fourier transform infrared (FT-IR) spectrum of the samples were recorded in the wave number range of 400-4000 cm^{-1} using a Nicolet 380 spectrometer (Thermoscientific, USA). The surface morphology analysis of the materials was performed by field emission scanning electron microscopy (FESEM) (FEI-Sirion200, Netherlands), transmission electron microscopy (TEM, JEOL-2010, Japan), field emission transmission electron microscopy (FEI-Tecnai G2 F30 S-TWIN, USA), X-ray photoelectron spectroscopy

(XPS, Thermo ESCALAB 250XI, USA). The electromagnetic parameters were measured at room temperature using a vector network analyzer (VNA, AV3629D, China) in the 2-18 GHz frequency range. Coaxial specimens for electromagnetic parameters were prepared by uniformly dispersing samples in molten paraffin wax, and then molding into toroid-shaped samples with an outer diameter of 7.0 mm and inner diameter of 3.0 mm. The weight ratio of composite with paraffin wax was 3:1.

3 Results and discussion

3.1 Schematic illustration of the synthesis procedure

Fig. 1 shows a schematic illustration of the synthesis process of Ni-doped SnO_2@MWCNTs composites. After reflux at 120 ^oC for 6 h in concentrated HNO_3, some functional groups, such as -COOH and -OH groups, and defects could be generated on the MWCNTs surfaces. These functional groups and defects provided locations for the deposition of Sn^{4+} and Ni^{2+}. After hydrothermal treatment at 160 ^oC for 18 h, the SnO_2 nanocrystals were in situ generated on the surface of MWCNTs due to the electrostatic interactions between Sn^{4+} and the functional groups and thus the Ni-doped SnO_2@MWCNTs composites were obtained.

3.2 Morphological analysis

Fig. 2(a) and (b) show the typical SEM images of MWCNTs and SnO_2@MWCNTs composites. From Fig. 2(a), it can be seen that the smooth morphology of outer surface of the MWCNTs. As shown in Fig. 2(b), some particles are dispersed in MWCNTs matrix, however, it is hardly determine the morphology and size. Fig. 2(c)~(e) present the typical TEM images of MWCNTs, SnO_2@MWCNTs and Ni-doped SnO_2@MWCNTs composites, respectively. Fig. 2(c) shows that the MWCNTs has an outer diameters around 50-60 nm and an inner diameters about 10

nm and length in several micrometers, respectively. As shown in Fig. 2(d), very fine SnO_2 nanoparticles are deposited onto the surfaces of MWCNTs. The aggregation of SnO_2 nanoparticles are hardly observed and they are uniformly distributed on the surface of MWCNTs with a diameter in the range of 3-5 nm. Fig. 2(e) and (g) depict that after doping with nickel ions (Ni^{2+}), SnO_2 nanoparticles are much more densely loaded on MWCNTs surfaces compared with un-doped SnO_2@MWCNTs in Fig. 2(d).

Fig. 2(f) shows the EDS elemental composition of Ni-doped SnO_2@MWCNTs composites. It is clearly shows that the peaks associated with C, Sn, Ni, O elements are present. The HRTEM image of Ni-doped SnO_2@MWCNTs composites shown in Fig. 2(h) also reveals the crystalline structure of the composites, and the crystalline lattice spacing (0.35 nm) and (0.22 nm) can be assigned to the (110) plane and (220) plane of SnO_2, respectively. Based on the TEM and HRTEM analysis, it can be seen that the structure of SnO_2@MWCNTs was not changed, and Ni ions has successfully doped into SnO_2@MWCNTs.

3.3 Structural analysis

The crystal structure of Ni-doped SnO_2@MWCNTs composites with different doped Ni contents was characterized by XRD, as shown in Fig. 3(a). The three typical diffraction peaks at 2θ = 26.5°, 33.8°, 51.6° can be assigned to the (110), (101), (211) crystal planes of SnO_2, respectively (JCPDS 41-1445).[19] The broad diffraction peak at 2θ = 26.5° (110) plane of SnO_2 overlapped with the peak of the graphitic reflection from MWCNTs. The average crystalline size can be estimated by Scherrer′s formula[25]:

$$D = \frac{K\lambda}{\beta \cos\theta} \quad (1)$$

Where D is the grain diameter, K (0.89) is the shape factor, λ is the X-ray wavelength of Cu Kα radiation (0.154 nm), θ is the Bragg angle, and β is the experimental full-width half-maximum of the respective diffraction peak. Therefore, the calculated average diameter of SnO_2 nanoparticles was about 3-5 nm, which is in accordance with the results of TEM images.

To explore the effect of doped Ni content on the crystalline structure of Ni-doped SnO_2@MWCNTs composites, the (101) and (211) characteristic diffraction peaks are monitored. From Fig. 3(b), it can be apparently seen that as the doped Ni molar percentage increases from 0 to 35.4%, the 2θ of (101) and (211) diffraction peaks shift right from 0.15° to 0.85° and from 0.55° to 1.86°, respectively. Besides, the plane of (101) intensity decreases and the plane of (200) enhances with the doping percentage increasing. However, there is no characteristic diffraction peaks of Ni species can be detected, which may be due to the high dispersion of the Ni nanoparticles with too small particle sizes to be identified by the conventional XRD method. When the Ni doping percentage more than 35.4%, the XRD results are showed in the supplement information. Additionally, the lattice constant a and c of Ni-doped SnO_2@MWCNTs composites exhibit in Table 1. According to the lattice parameters of the composites, the lattice constant a and c are changing when Ni ions doping into SnO_2@MWCNTs. Because the ion radius of Ni^{2+} (0.69 Å) is smaller than that of Sn^{4+} (0.71 Å), the decrease of lattice constant of SnO_2@MWCNTs is caused by the substitution of Sn atoms of SnO_2 lattice by Ni atoms. So the lattice constant of Ni-doped SnO_2@MWCNTs with different Ni molar percentage are less than the SnO_2@MWCNTs lattice constant values (a=b=4.76930, c=3.16126).[26] Combined the

results of EDS, XRD and HRTEM analysis, it can be deduced that the Ni^{2+} cation have systematically entered the crystal lattice of SnO_2 without deteriorating the original crystal structure. Therefore, the Ni-doped SnO_2@MWCNTs composites were successfully synthesized by a facile hydrothermal method.

In order to confirm the presence of the surface compositions and chemical state of MWCNTs, XPS was carried out to further confirmation. Fig. 3(c) shows the wide span spectra of SnO_2@MWCNTs and Ni-doped SnO_2@MWCNTs composites, which indicates that these two spectra are the same except the Ni peaks were arose in the latter one. In Fig. 3(d), the spectrum of C 1s shows four peaks at 284.6 eV, 285.6 eV, 286.7 eV and 288.9 eV, corresponding to C-C or C=C in the aromatic rings, C-O, C=O, and O-C=O groups of acid MWCNTs, respectively.[27] The O 1s peaks at 531.0 eV, 531.6 eV and 532.8 eV shown in Fig. 3(e), referring to C=O or O-Sn-O group, the absorbed oxygen within the crystalline and C-O in the MWCNTs.[27,28]For the spectrum of Sn in Fig. 3(f), the peaks of Sn are loaded at 487.5 eV and 495.9 eV, which are assigned to Sn $3d_{5/2}$ and Sn $3d_{3/2}$. The energy gap of Sn $3d_{3/2}$ and Sn $3d_{5/2}$ is 8.4 eV, and this spin-orbit splitting is assigned to the lattice of Sn^{4+} ions in tin oxide.[29,30] In terms of Ni element chemical state, Fig. 3(g) exhibit the spectrum of Ni in Ni-doped SnO_2@MWCNTs composites. The peaks at 856.6 eV and 862.6 eV are assigned to Ni $2p_{3/2}$ and its satellite structure, while peaks at 874.3 eV and 880.5 eV are attributed to Ni $2p_{1/2}$ and its satellite structure. Herein, the energy difference between Ni $2p_{1/2}$ and Ni $2p_{3/2}$ is 17.7 eV, which is different from that of NiO (18.4 eV),[31,32] suggesting that the Ni ions is present in SnO_2@MWCNTs. Besides, among the broad peak at 862.6 eV, there are two low shoulder peaks at 861.4 eV and 864.2 eV, indicating Ni-O binding is present in Ni-doped SnO_2@MWCNTs. The Ni-O binding is from the substitution of Ni ion to Sn^{4+}. According to integral area and the atomic ratio of Ni to

the whole composites (4.59%), the amount of Ni-O binding is estimated to be about 2%. Meanwhile, XPS also show the C, Sn, O elements in the SnO_2@MWCNTs, while C, Sn, Ni, O elements in the Ni-doped SnO_2@MWCNTs, which consistent with the EDS results. Considering these results above, indicates that the doping of Ni ions substituted Sn site of the lattice and Ni-O binding was exiting in the Ni-doped SnO_2@MWCNTs.

3.4 FT-IR spectra

Fig. 4 depicts the FT-IR spectra of MWCNTs, SnO_2@MWCNTs, and Ni-doped SnO_2@MWCNTs, respectively. The FT-IR spectrum of MWCNTs confirmed the presence of oxygen-containing groups, such as C-OH at 3440 cm^{-1}, and C=O in the carboxylic acid moieties at 1744 cm^{-1}. Other characteristic vibrations were the O-H deformation peak at 1640 cm^{-1}, the C-O stretching peak at 1079 cm^{-1}, and the C-H in-plane bending vibration peak at 1383 cm^{-1}. The appearance of peaks at 2928 and 2860 cm^{-1} correspond to C-H asymmetric stretching of the $-CH_3$ and $-CH_2$ group. The SnO_2@MWCNTs composites has similar FT-IR spectrum as MWCNTs. The characteristic band at 608 cm^{-1} is assigned to the stretching of O-Sn-O vibration, which indicates that the incorporation of SnO_2 particles on the MWCNTs. Ni-doped SnO_2@MWCNTs composites have similar FT-IR spectrum as SnO_2@MWCNTs. However, the strength of absorbing peaks around 400-800 cm^{-1} in Ni-doped SnO_2@MWCNTs significantly decreases due to the Ni^{2+} doping.

3.5 Raman spectra

Raman spectroscopy is a powerful and non-destructive technique for the characterization of interactions or bonding between two components.[19,33,34] Fig. 5

shows the Raman spectra of MWCNTs, SnO_2@MWCNTs and Ni-doped SnO_2@MWCNTs composites, respectively. It is notably showed that all the three samples present three characteristic peaks, namely the D band (~1350 cm^{-1}), the G band (~1580 cm^{-1}) and the 2D band (~2700 cm^{-1}), which correspond to the first-order vibration of sp^3 bond, the in-plane vibration of sp^2 bond and the second-order vibration of sp^3 bond, respectively.[19] Moreover, the interactions between the MWCNTs and SnO_2 nanoparticles are clearly shown by the slight red shift in the peaks of MWCNTs from 1355 to 1351 cm^{-1} in the D band and from 2708 to 2704 cm^{-1} in the 2D band.[19] The I_D/I_G (strength ratio of D band to G band) value decreases from 0.85 to 0.78 after SnO_2 nanoparticles were deposited on the surface of MWCNTs, which may be due to the defects on the surface of MWCNTs were covered by SnO_2 nanoparticles.[35] Significantly, the Raman spectra of Ni-doped SnO_2@MWCNTs composites shows slight blue shift compared with SnO_2@MWCNTs composites. The peaks at D band shifts from 1351 to 1358 cm^{-1} and the 2D band from 2704 to 2711 cm^{-1}. The I_D/I_G value increased from 0.78 to 0.88, indicating that the interactions between MWCNTs and SnO_2 become stronger as the doping of Ni^{2+}. Interestingly, the G band remains the same peak at 1581 cm^{-1} for all three samples. It can be deduced that the introduction of SnO_2 and Ni^{2+} do not change the structure of the MWCNTs, and Ni^{2+} had successfully doped into SnO_2@MWCNTs.

3.6 Microwave absorbing properties

The microwave absorbing properties of Ni-doped SnO_2@MWCNTs can be characterized by the parameter reflection loss *RL*. According to the transmission line theory, *RL* can be calculated by the following equations:[35,36,37]

$$RL(dB) = 20\lg\left|\frac{Z_{in}-1}{Z_{in}+1}\right| \quad (2)$$

$$Z_{in} = \sqrt{\frac{\mu_r}{\varepsilon_r}}\tanh\left[j\left(\frac{2\pi fd}{c}\right)\sqrt{\frac{\mu_r}{\varepsilon_r}}\right] \quad (3)$$

Where Z_{in} is the input impedance of absorber, d is the thickness of the absorber, and c and f are the velocity of light and the frequency of microwave, respectively. $\varepsilon_r = \varepsilon' - j\varepsilon''$ and $\mu_r = \mu' - j\mu''$ are the complex permittivity and complex permeability of the absorber material, respectively.

As illustrated in Fig. 6(a), for Ni-doped SnO_2@MWCNTs composites with different doped Ni molar percentage, the values of real permittivity ε' tend to decrease with the increase of frequency over the whole frequency range (2-18 GHz). The values of ε' are in the range of 9.96 to 25.46 from 0% to 35.4% doped Ni molar percentage, respectively. Meanwhile, in Fig. 6(b), the imaginary permittivity ε'' values of Ni-doped SnO_2@MWCNTs composites is fluctuating in the range of 2-18 GHz, which first declines, and then increases with three peaks. The values of ε'' are in the range of 4.29 to 15.67 from 0% to 35.4% doped Ni molar percentage, respectively. It is well known that high value of ε' is harmful to the microwave absorption, which might lead to the impedance mismatch. The high values of ε' of Ni-doped SnO_2@MWCNTs might come from interfacial polarization, which may results from the SnO_2 nanoparticles deposit on the surface of MWCNTs. Combined Fig. 6(a) with (b), it can be seen that the Ni-doped SnO_2@MWCNTs composites with 10.7% doped Ni molar percentage, both the ε' and ε'' curves are much higher than any other composites, indicating the worst impedance mismatching characteristic.

Fig. 6(c) and (d) show the real permeability μ' and imaginary permeability μ'' curves of Ni-doped SnO_2@MWCNTs composites with different doped Ni molar

percentage, respectively. It is found that in Fig. 6(c), the values of μ' are in the range of 0.92 to 1.39 from 0% to 35.4% doped Ni molar percentage, respectively, almost fluctuating around the constant 1 ($\mu' \approx 1$). As shown in Fig. 6d, the values of μ'' are in the range of -0.44 to 0.23 from 0% to 35.4% doped Ni molar percentage, respectively, fluctuating around the constant 0 ($\mu'' \approx 0$).

In general, magnetic loss mainly come from eddy current effects, natural resonance, and exchange resonance in the microwave frequency. The eddy current effects is related to the thickness (d) and the electrical conductivity (σ) of the material, which can be calculated by the equation[38,39]:

$$\mu'' \approx 2\pi\mu_0(\mu')^2\sigma d^2 f / 3 \quad (4)$$

where μ_0 is the permeability of vacuum. From the equation, if magnetic loss only come from eddy current effects, the values of $\mu''(\mu')^{-2}f^{1}$ should be constant when frequency is varied. However, as demonstrated in Fig. 6(e), the values $\mu''(\mu')^{-2}f^{1}$ of Ni-doped SnO_2@MWCNTs show some peaks, which means that the magnetic loss is not mainly originated from eddy current effects as the Ni-doped SnO_2@MWCNTs composites showing little magnetic loss.[39]

To further demonstrate the microwave absorbing properties of Ni-doped SnO_2@MWCNTs composites, the dielectric loss tangent ($\tan\delta_e = \varepsilon''/\varepsilon'$) and magnetic loss tangent ($\tan\delta_m = \mu''/\mu'$) are plotted against frequency, respectively. As illustrated in Fig. 6(f), the values of $\tan\delta_e$ for the Ni-doped SnO_2@MWCNTs composites change from 0.34 to 0.93 from 0% to 35.4% doped Ni molar percentage, respectively. Meanwhile, when the doped Ni molar percentage is less than 10.7%, the values of $\tan\delta_e$ are higher than that of SnO_2@MWCNTs. However, when the doped Ni molar percentage is more than 10.7%, the values of $\tan\delta_e$ become lower than that

of SnO_2@MWCNTs. These results suggest that the Ni-doped SnO_2@MWCNTs composites have distinct dielectric loss properties with different doped Ni molar percentage. Fig. 6 (g) shows that the values of $\tan\delta_m$ change from -0.38 to 0.21 from 0% to 35.4% doped Ni molar percentage, respectively. Comparing Fig. 6(f) with (g), it can be obviously observed that the values of $\tan\delta_e$ are much higher than $\tan\delta_m$ for all samples, indicating that Ni-doped SnO_2@MWCNTs composites are a kind of dielectric loss types microwave absorbing materials.

Additionally, effective microwave absorber should accord to two factors. One is the impedance matching between the complex permittivity and the complex permeability, the other is electromagnetic microwave attenuation of the microwave absorber. Yet, the EM was determined by the attenuation constant α, suggesting in the following equation[39,40]:

$$\alpha = \frac{\sqrt{2}\pi f}{c} \times \sqrt{(\mu''\varepsilon'' - \mu'\varepsilon') + \sqrt{(\mu''\varepsilon'' - \mu'\varepsilon')^2 + (\mu''\varepsilon'' + \mu'\varepsilon')^2}} \quad (5)$$

where f is the EM-wave and c is the velocity of light. Fig. 6(h) shows the frequency dependence of the attenuation constant in the range of 2-18 GHz. Notably, it can be found that the Ni-doped the SnO_2@MWCNTs-paffin composites curves similarly each other. The high attenuation constant of the composites for different Ni ions molar percentage shows the excellent attenuation, but a high α value does not indicate a strong dielectric loss or magnetic loss,[40,41] which may result from the impedance mismatching especially for 10.7% molar percentage of Ni ions doping. While for the 28.2% molar percentage of Ni ions doping shows the best impedance matching, exhibiting the best microwave absorption.

To further understand the mechanism of dielectric loss of the microwave

absorber, the Debye dipolar relaxation is often related, permittivity can be expressed by the following equation:[1,37,42]

$$\varepsilon_r = \varepsilon_\infty + \frac{\varepsilon_s - \varepsilon_\infty}{1 + j2\pi f\tau} = \varepsilon' - j\varepsilon'' \quad (6)$$

Where ε_s, ε_∞, f, τ are the static permittivity, relative dielectric permittivity at high-frequency limit, frequency and polarization relaxation time, respectively. Therefore, ε' and ε'' can be deduced by:

$$\varepsilon' = \varepsilon_\infty + \frac{\varepsilon_s - \varepsilon_\infty}{1 + (2\pi f)^2 \tau^2} \quad (7)$$

$$\varepsilon'' = \frac{2\pi f\tau(\varepsilon_s - \varepsilon_\infty)}{1 + (2\pi f)^2 \tau^2} \quad (8)$$

According to eqn (7) and (8), the relationship between ε' and ε'' can be described as following:

$$\left(\varepsilon' - \frac{\varepsilon_s + \varepsilon_\infty}{2}\right)^2 + (\varepsilon'')^2 = \left(\frac{\varepsilon_s - \varepsilon_\infty}{2}\right)^2 \quad (9)$$

$$\varepsilon' = \frac{\varepsilon''}{2\pi f\tau} + \varepsilon_\infty \quad (10)$$

Based on eqn (9), the curves of (ε''~ε') would be a single semicircle, denoting as the Cole-Cole semicircle. Each semicircle represents one Debye relaxation process. Fig. 7 shows that there are at least three semicircles in each curve of Ni-doped SnO_2@MWCNTs with different doped Ni molar percentage. These results indicate that the Debye relaxation process can enhance the microwave absorbing properties of Ni-doped SnO_2@MWCNTs composites. However, the Cole-Cole semicircle are distorted, suggesting that other mechanisms such as conductance loss, interfacial polarization or oxygen defects may beneficial to the microwave absorption.[37,43]

Fig. 8(a) to (f) show the calculated *RL* curves of Ni-doped SnO_2@MWCNTs

composites of different Ni doped molar percentage with different matching thicknesses of microwave absorbing layer in the range of 2~18 GHz. It can be seen that the maximum *RL* towards the low frequency with the increase of thickness. Fig. 8(a) depicts that the maximum *RL* reaches -21.6 dB at 8.6 GHz for SnO_2@MWCNTs composites with a thickness of 2 mm. For 10.7% Ni-doped SnO_2@MWCNTs composites, the maximum *RL* can reach up to -14.7 dB at 3.7 GHz with a thickness of 1.5 mm as shown in Fig. 8(c). When the Ni doped molar percentage was 10.7%, the microwave absorbing properties was poor compared to the other five percentage composites, just because the mismatch between the absorber and the air. The maximum *RL* values is of small change when the Ni doped molar percentage less than 10.7% (Fig. 8(b)), while with the doping content increasing (Fig. 8(d) to (f)), the change of the maximum *RL* becomes larger, and the largest maximum *RL* belongs to 28.2% Ni doping percentage in Fig. 8(e). For 28.2% Ni-doped SnO_2@MWCNTs composites, the maximum *RL* reaches -39.2 dB at 8.2 GHz with the thickness of 2.5 mm. Further increases Ni doping percentage, however, the value of maximum *RL* changes slightly, and almost keep constant. Similarly, the widest microwave absorption located at 28.2% and 35.4% (Fig. 8(f)) Ni doping percentage, which can reach 3.6 GHz. Considering the maximum *RL* and the widest microwave absorption, the optimal doped Ni molar percentage is 28.2%, at which the Ni-doped SnO_2@MWCNTs composites presents the excellent microwave absorbing properties, possibly due to the best impedance match characteristic.

The possible mechanisms of microwave absorption for Ni-doped SnO_2@MWCNTs composites are schematic illustration in Fig. 9. On one hand, the small size of SnO_2 nanoparticles is about 3-5 nm, which can be act as polarization center, enhancing the interfacial polarization effect too.[44] Small size particles possess

high anisotropy, which also make contributions to the microwave absorption.[19] On the other hand, the Debye relaxation process is beneficial to attenuate the incident electromagnetic wave, and the high conductivity of MWCNTs plays an important role in the formation of conductive network.[3] Besides, Ni ions doping can make it easier to form a conductive network in SnO_2@MWCNTs composites. In addition, Ni ions doping can change the lattice parameters of SnO_2@MWCNTs, Ni ions substituted Sn^{4+} ions in the lattice of tin oxide, lattice deformation can be good for the microwave absorption of SnO_2@MWCNTs composites. Additionally, the large aspect ratio and the existence of residual defects and groups of the Ni-doped SnO_2@MWCNTs composites could cause multiple reflections,[45] which will further enhance the microwave absorbing ability. In general, the enhanced microwave absorbing performance of the composites is attributed to the synergistic effects of the MWCNTs, Ni ions, and SnO_2 nanoparticles. Only with impedance match, high conductivity, high attenuation and reduced eddy current of the three components can make Ni-doped SnO_2@MWCNTs composites have better microwave absorbing properties. Therefore, the Ni-doped SnO_2@MWCNTs composites have a great potential as lightweight and high-efficiency electromagnetic wave absorbers.

4. Conclusions

In summary, the Ni-doped SnO_2@MWCNTs composites were synthesized by a facile one-step hydrothermal method. XRD and TEM analysis demonstrated that SnO_2 nanoparticles were successfully anchored on the surface of MWCNTs with a diameter of 3-5 nm. Raman spectra results indicated that the interactions between MWCNTs and SnO_2 became stronger as the doping of Ni^{2+} and the Ni^{2+} had successfully doped into SnO_2@MWCNTs composites. The Ni-doped SnO_2@MWCNTs composites with

28.2% doped Ni molar percentage showed the best microwave absorbing properties, i.e. the maximum *RL* reached -39.2 dB at 8.2 GHz with a thickness of 2.5 mm and the bandwidth of $RL \leq -10$ dB was 3.6 GHz at the thickness of 1.5 mm. It was believed that the Ni-doped SnO_2@MWCNTs composites were attractive candidates for light weight and high-efficiency electromagnetic wave absorbers.

Acknowledgements

This work was financially supported by the Natural Science Foundation of China (Grant No. 51477002; 51507003; 51173002) and the Doctor's Start-up Research Foundation of Anhui University of Science and Technology.

Fig. Captions

Fig. 1 A schematic illustration of the synthesis process of Ni-doped SnO_2@MWCNTs composites.

Fig. 2 SEM images of MWCNTs (a) and SnO_2@MWCNTs composites (b), TEM images of MWCNTs (c), SnO_2@MWCNTs composites (d) and Ni-doped SnO_2@MWCNTs composites (e) and (g), the EDS spectrum of Ni-doped SnO_2@MWCNTs composites (f), and HRTEM image of Ni-doped SnO_2@MWCNTs (h).

Fig. 3 XRD patterns of Ni-doped SnO_2@MWCNTs composites with different doped Ni molar percentage at 2θ = 10-80° (a) and at 2θ = 30-55° (b).

XPS spectra of SnO_2@MWCNTs and Ni-doped SnO_2@MWCNTs composites: wide span (c), C 1s spectrum (d), O 1s spectrum (e), Sn 3d spectrum (f) and Ni2p spectrum of Ni-doped SnO_2@MWCNTs composites (g).

Table. 1 Lattice constant of Ni-doped SnO_2@MWCNTs composites with different Ni molar percentange.

Fig. 4 FT-IR spectra of MWCNTs, SnO_2@MWCNTs composites and Ni-doped SnO_2@MWCNTs composites.

Fig. 5 Raman spectra of MWCNTs, SnO_2@MWCNTs composites and Ni-doped SnO_2@MWCNTs composites.

Fig. 6 Frequency dependence on real parts (a) and imaginary parts (b) of the complex permittivity, real parts (c) and imaginary parts (d) of the complex permeability, the value of $\mu''(\mu')^{-2}f^{1}$ of Ni-doped SnO_2@MWCNTs composites with different doped Ni molar percentage as a function of frequency (e), and the dielectric loss tangents tan δ_e (f) and magnetic loss tangents tan δ_m (g) of Ni-doped SnO_2@MWCNTs composites with different doped Ni molar percentage, attenuation constant of Ni-doped

SnO_2@MWCNTs-paraffin composites with different doped Ni molar percentage versus frequency (h).

Fig. 7 $\varepsilon' \sim \varepsilon''$ curves of Ni-doped SnO_2@MWCNTs composites with different doped Ni molar percentage.

Fig. 8 Reflection losses for Ni-doped SnO_2@MWCNTs composites with different doped Ni molar percentage at different thicknesses in the frequency range of 2-18 GHz.

Fig. 9 Schematic illustration of possible microwave absorption mechanisms of Ni-doped SnO_2@MWCNTs composites.

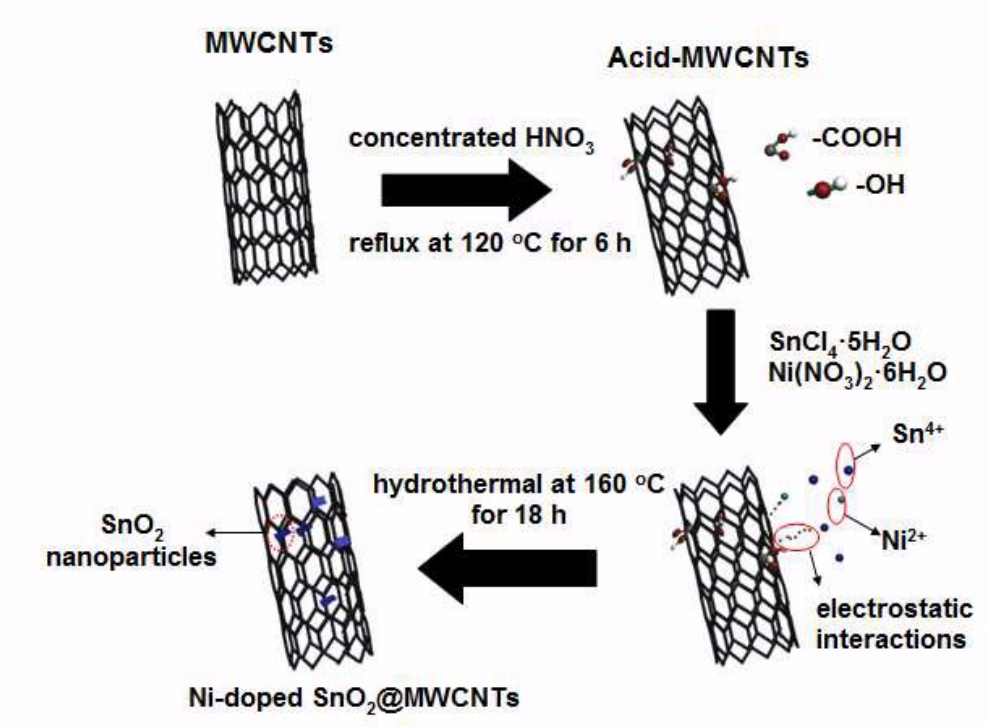

Fig. 1

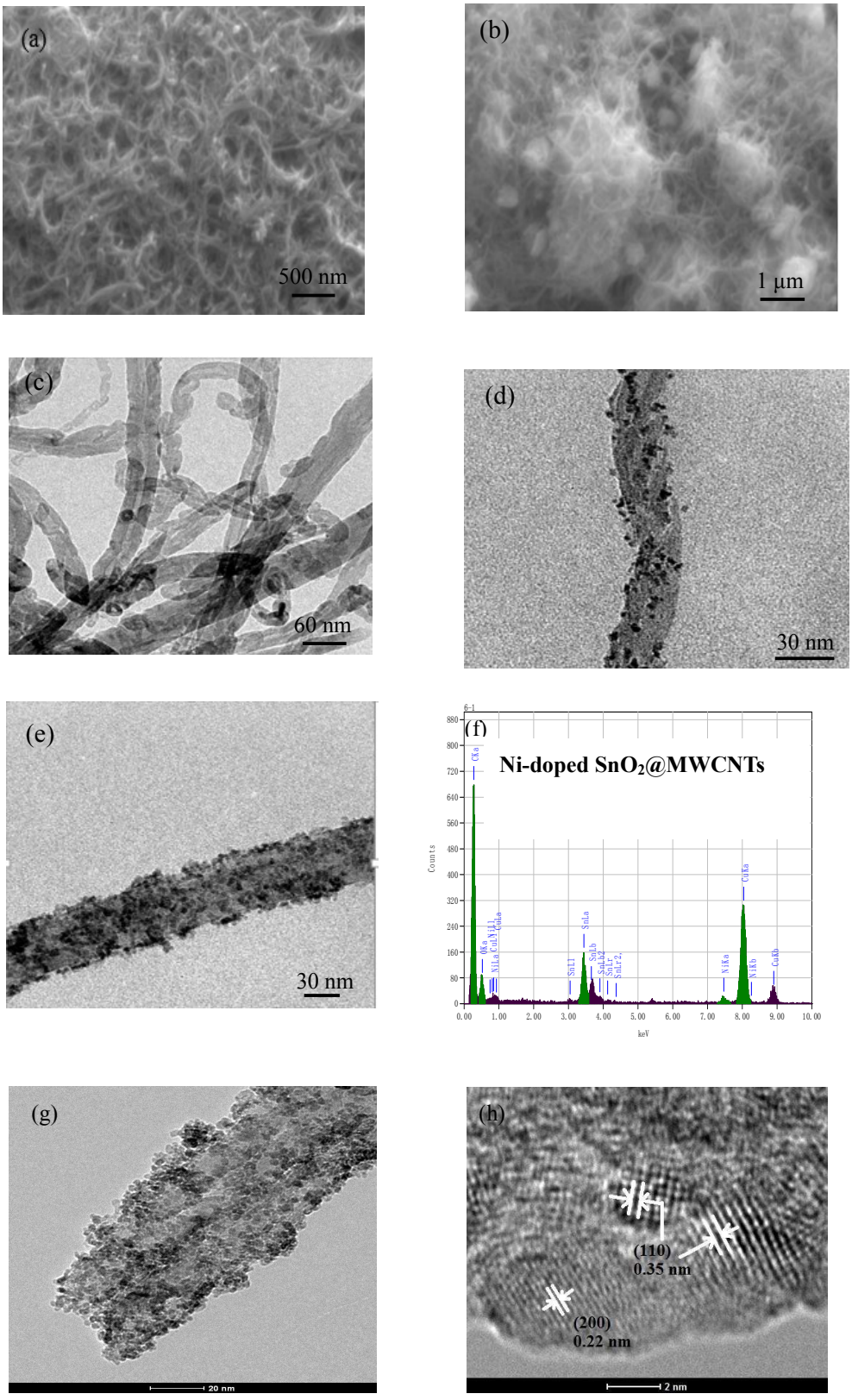

Fig. 2

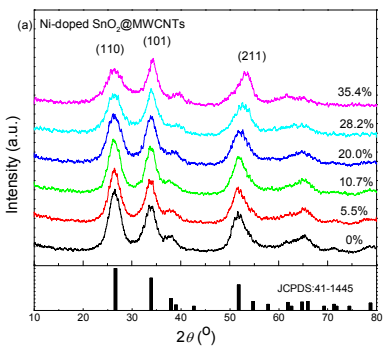

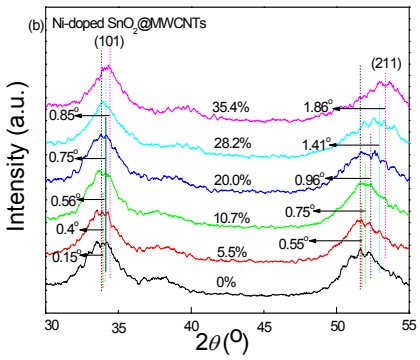

Samples	Lattice constant/(Å)	
	a=b	c
0% Ni-doped SnO_2@MWCNTs	4.76930	3.16126
5.5% Ni-doped SnO_2@MWCNTs	4.73722	3.18232
10.7% Ni-doped SnO_2@MWCNTs	4.74240	3.18576
20.0% Ni-doped SnO_2@MWCNTs	4.72681	3.19510
28.2% Ni-doped SnO_2@MWCNTs	4.73879	3.18593
35.4% Ni-doped SnO_2@MWCNTs	4.73742	3.18841

Table. 1

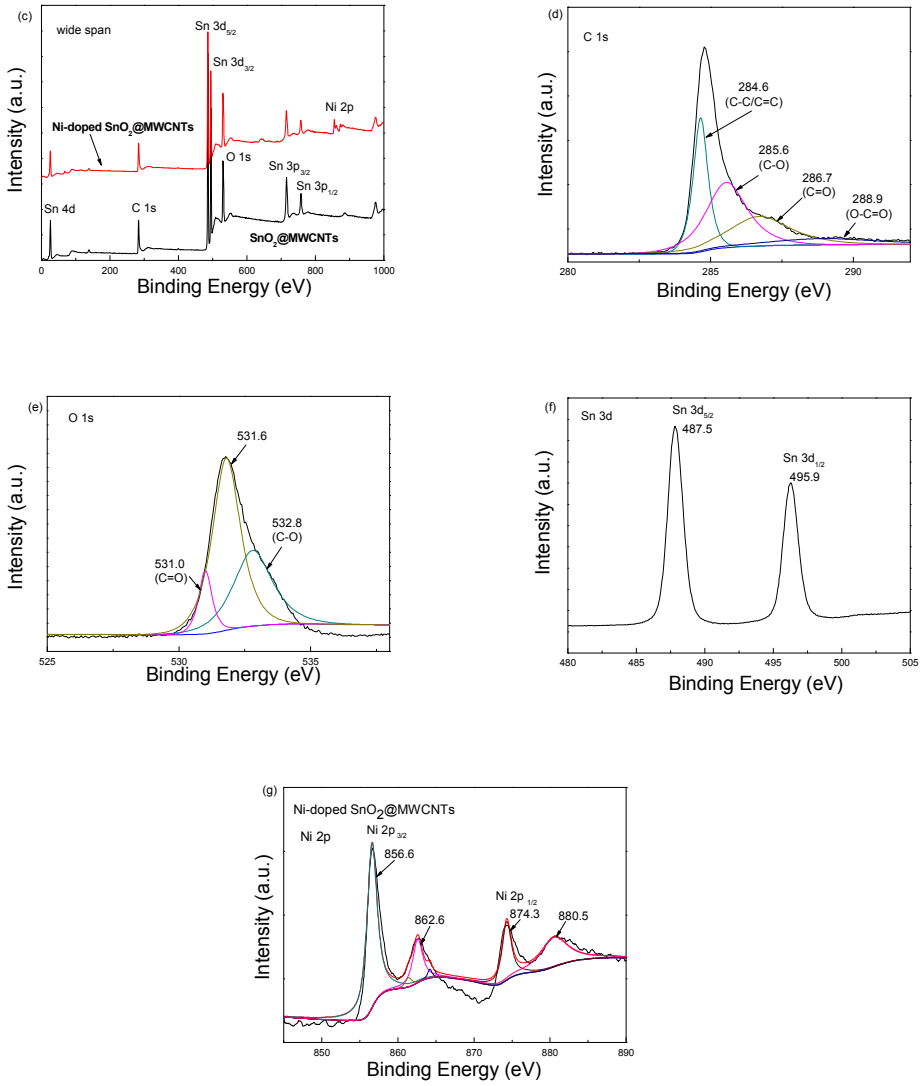

Fig. 3

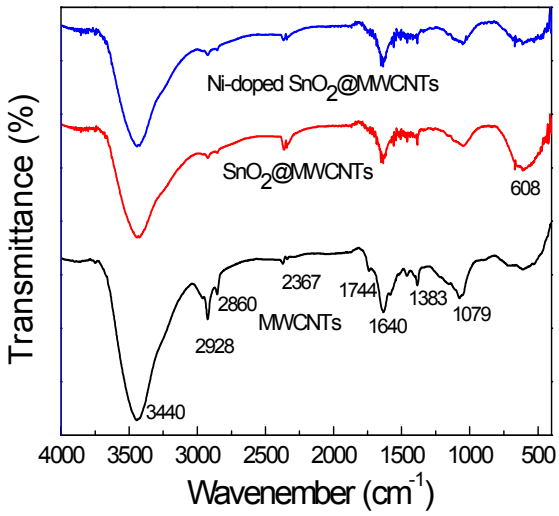

Fig. 4

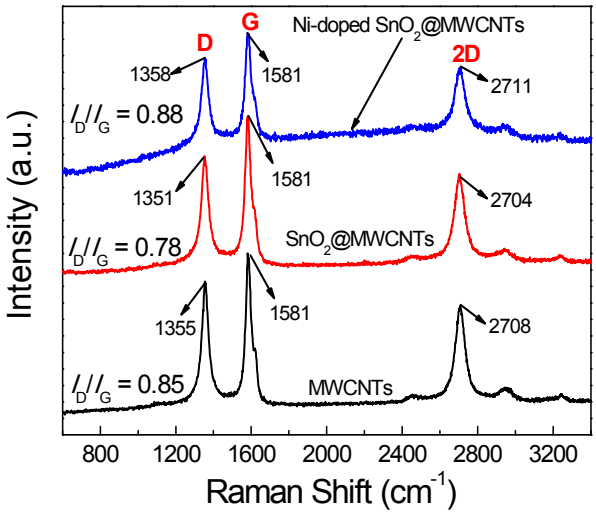

Fig. 5

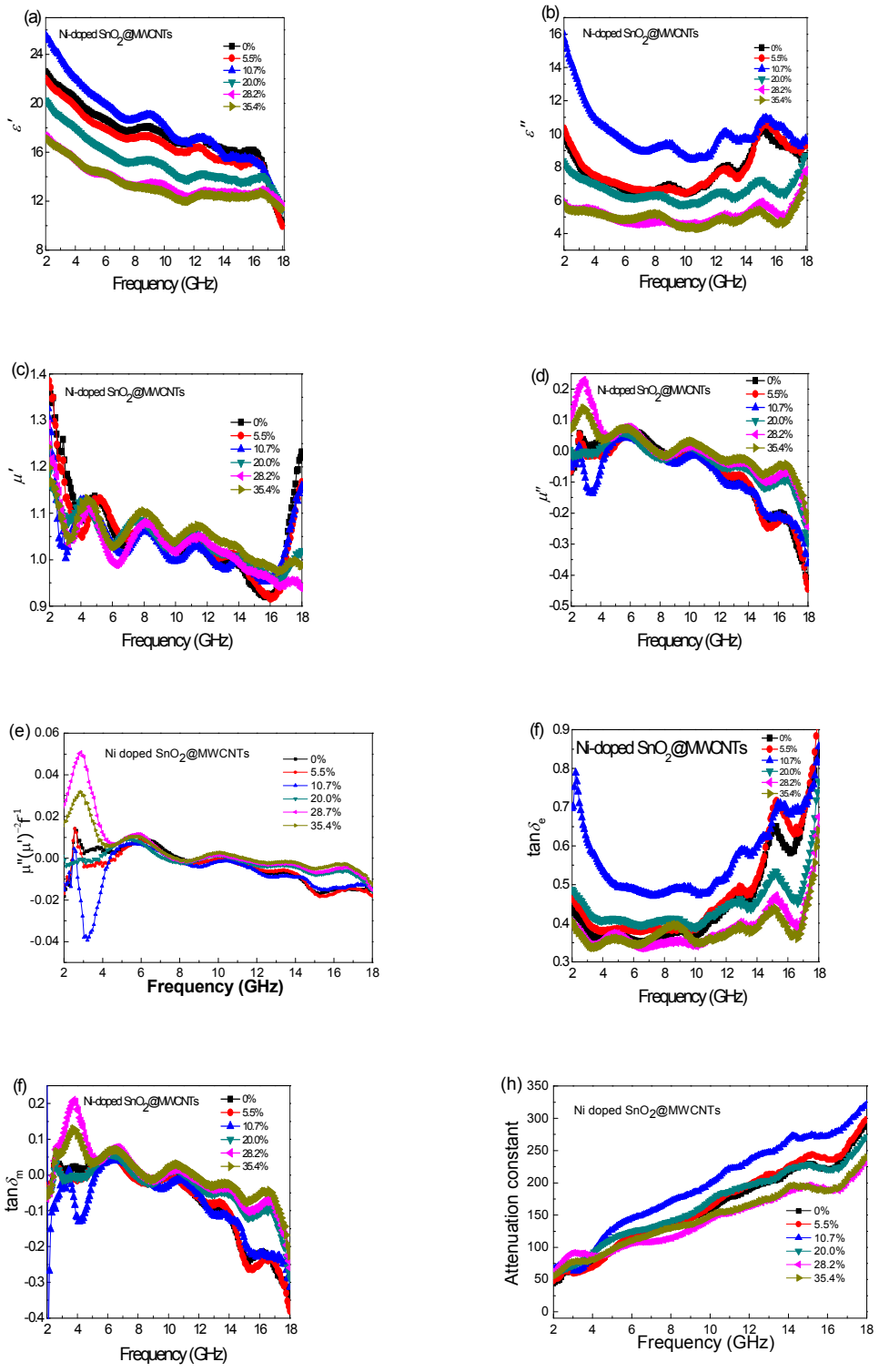

Fig. 6

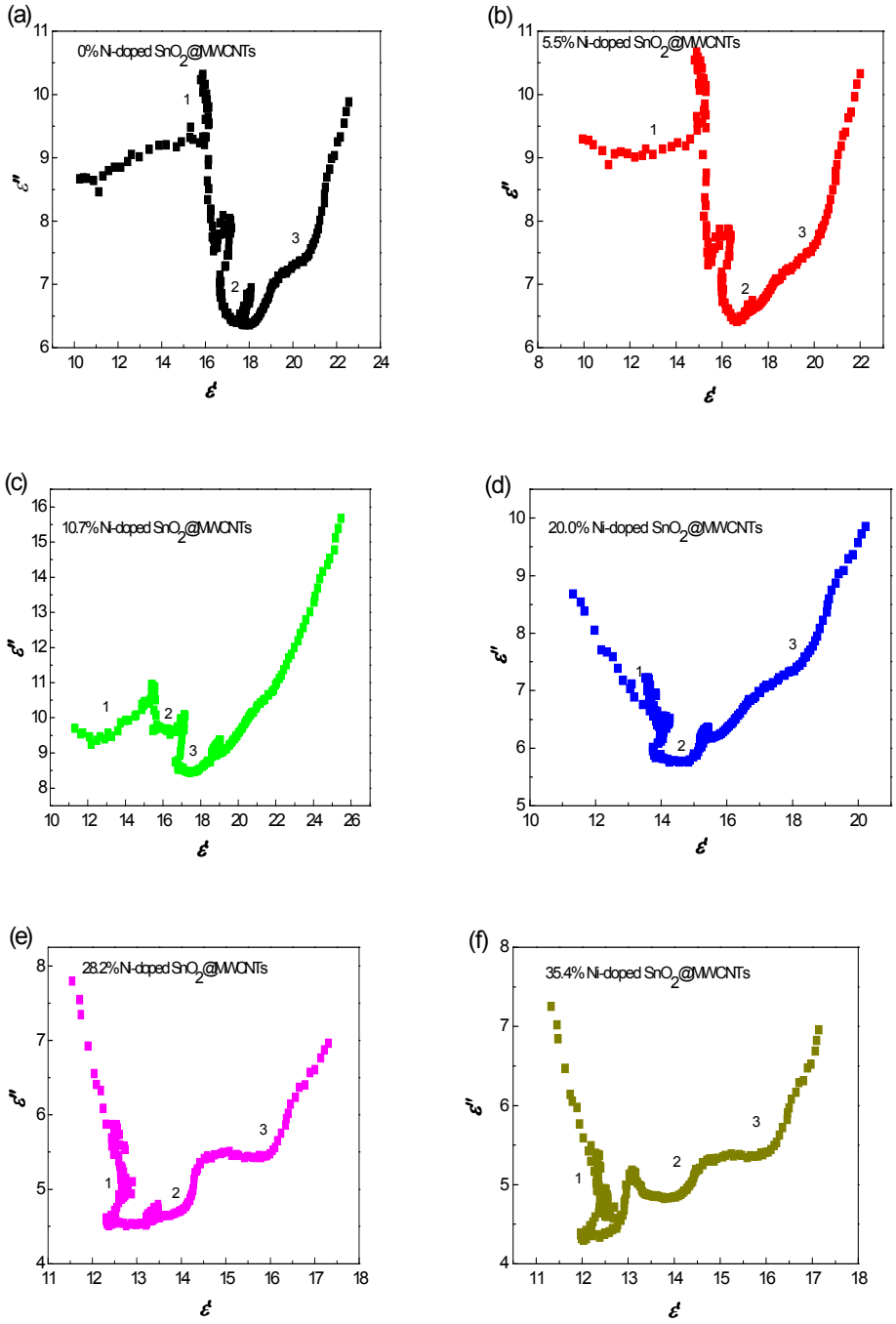

Fig. 7

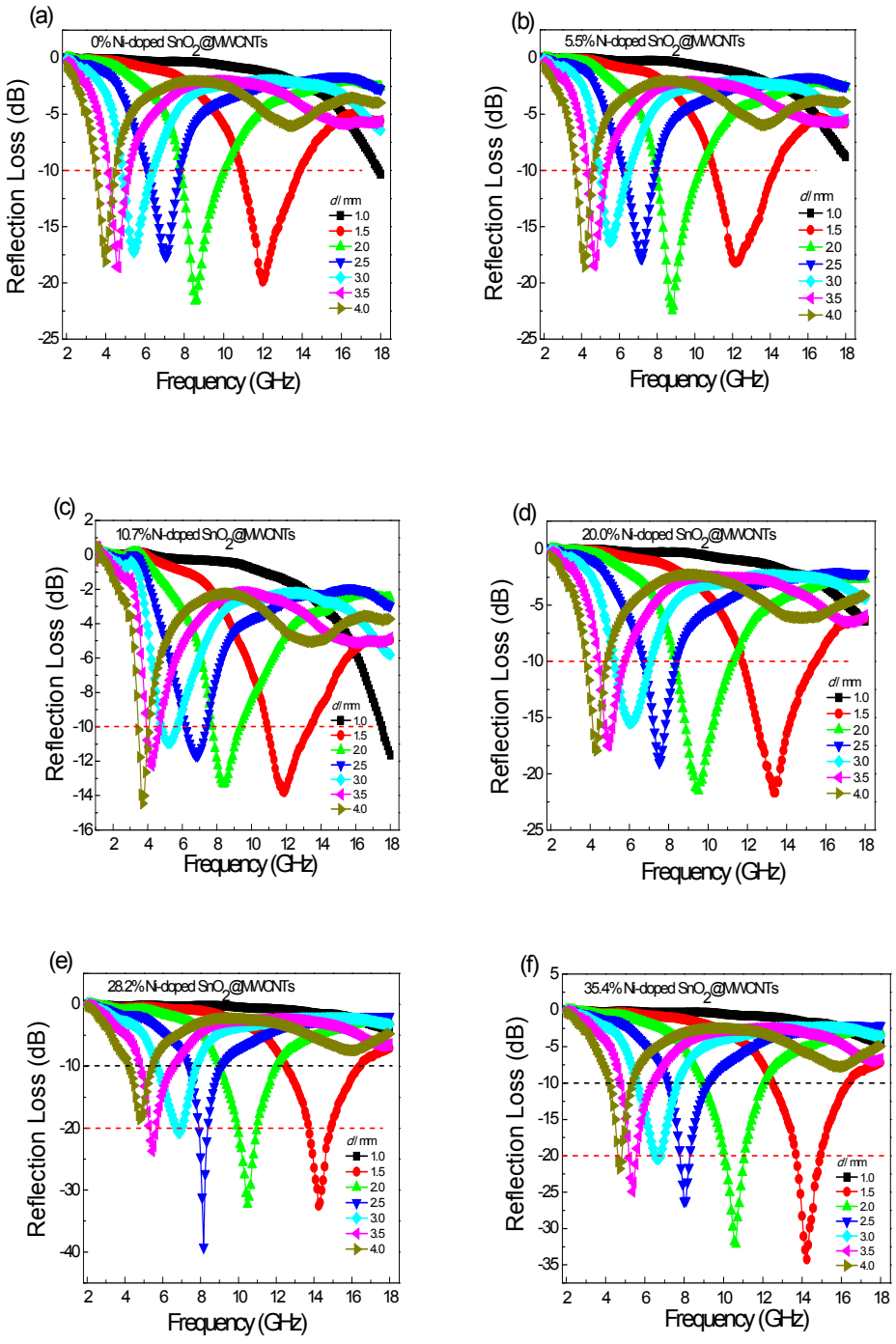

Fig. 8

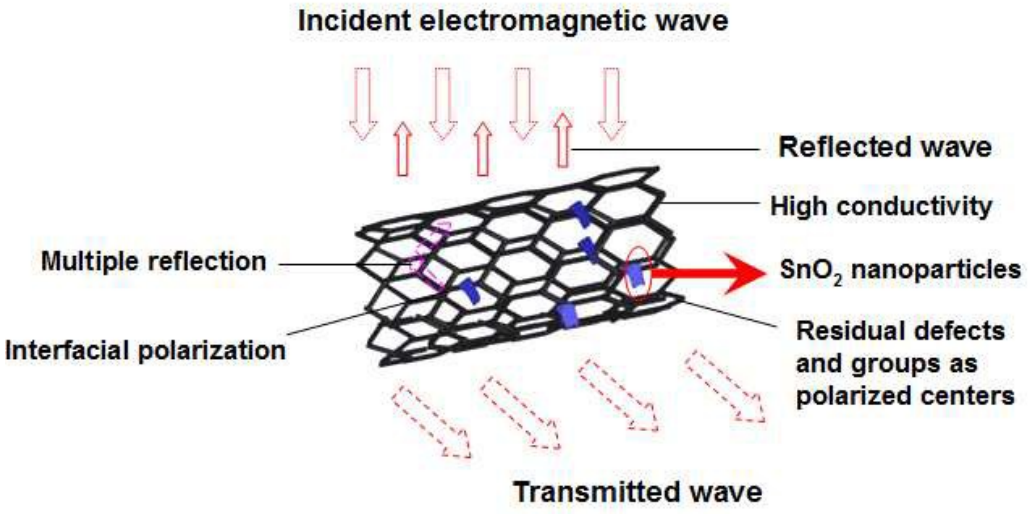

Fig. 9

Notes and references

1 D. Chen, G. S. Wang, S. He, J. Liu, L. Guo and M. S. Cao, *J. Mater. Chem. A*, 2013, **1**, 5996-6003.

2 P. B. Liu, Y. Huang and X. Sun, *ACS Appl. Mater. Interf.*, 2013, **5**, 12355-12360.

3 M. M. Lu, W. Q. Cao, H. L. Shi, X. Y. Fang, J. Yang, Z. L. Hou, H. B. Jin, W. Z. Wang, J. Yuan and M. S. Cao, *J. Mater. Chem. A*, 2014, **2**, 10540-10547.

4 Y. Danlée, I. Huynen and C. Bailly, *Appl. Phys. Lett.*, 2012, **100**, 213105.

5 F. Ren, H. Yu, L. Wang, M. Saleem, Z. Tian and P. Ren, *RSC Adv.*, 2014, **4**, 14419-14431.

6 T. Zhao, C. Hou, H. Zhang, R. Zhu, S. She, J. Wang, T. Li, Z. Liu and B. Wei, *Sci. Rep.*, 2014, **4**, 5619.

7 R. Che, L. M. Peng, X. F. Duan, Q. Chen and X. Liang, *Adv. Mater.*, 2004, **16**, 401-405.

8 X. Qi, W. Zhong, C. Deng, C. Au and Y. Du, *Mater. Lett.*, 2013, **107**, 374-377.

9 Z. Wang, L. Wu, J. Zhou, W. Cai, B. Shen and Z. Jiang, *J. Phys. Chem. C*, 2013, **117**, 5446-5452.

10 M. S. Cao, J. Yang, W. L. Song, D. Q. Zhang, B. Wen, H. B. Jin, Z. L. Hou and J. Yuan, *ACS Appl. Mater. Interf.*, 2012, **4**, 6949-6956.

11 X. X. Wang, M. M. Lu, W. Q. Cao, B. Wen and M. S. Cao, *Mater. Lett.*, 2014, **125**, 107-110.

12 B. Zhao, W.Y. Zhao, G. Shao, B.B. Fan and R. Zhang, *Dalton Trans.*, 2015, **44**,

15984-15993.

13 S. Gubbala, V. Chakrapani, V. Kumar and M. K. Sunkara, *Adv. Funct. Mater.*, 2008, **18**, 2411-2418.

14 H. C. Wu, Y. C. Huang, I. Ding, C. C. Chen, Y. H. Yang, C. C. Tsai, C. D. Chen and Y. T. Chen, *Adv. Funct. Mater.*, 2011, **21**, 474-479.

15 H. S. Oh, H. N. Nong and P. Strasser, *Adv. Funct. Mater.*, 2015, **25**, 1074-1081.

16 S. Javaid, M. A. Farrukh, I. Muneer, M. Shahid, M. Khaleep-ur-Rahman, A. A. Umar, *Superlattices and Microstructures*., 2015, **82**, 234-247.

17 H. Wang, K. Dou, W. Y. Teoh, Y. Zhan, T. F. Hung, F. Zhang, J. Xu, R. Zhang and A. L. Rogach, *Adv. Funct. Mater.*, 2013, **23**, 4847-4853.

18 P. Manjula, R. Boppella and S. V. Manorama, *ACS Appl. Mater. Interf.*, 2012, **4**, 6252-6260.

19 M. Mishra, A. P. Singh, B. P. Singh and S. Dhawan, *RSC Adv.*, 2014, **4**, 25904-25911.

20 J. Liu, J. Cheng, R. Che, J. Xu, M. Liu and Z. Liu, *J. Phys. Chem. C*, 2012, **117**, 489-495.

21 Y. J. Chen, P. Gao, R. X. Wang, C. L. Zhu, L. J. Wang, M. S. Cao and H. B. Jin, *J. Phys. Chem. C*,2009, **113**, 10061-10064.

22 B. Zhao, G. Shao, B. B. Fan, W. Y. Zhao and R. Zhang, *RSC Adv*., 2014, **4**, 57424-57429.

23 B. Zhao, G. Shao, B. B. Fan, W. Y. Zhao and R. Zhang, *Phys. Chem. Chem. Phys*., 2015, **17**, 2531-2539.

24 M. Kuppan, S. Kaleemulla, N. Madhusudhana Rao, N. Sai Krishna, M. Rigana Begam and M. Shobana, *Adv. In Condensed Matter Phys*., 2014, 1-5.

25 D. D. Han, N. R. Xiao, H. Hu, B. Liu, G. X. Song and H. Yan, *RSC. Adv*., 2015, **5**, 66667-66673.

26 X. Su, Y. Jia, X. Liu, J. Wang, J. Xu, X. He, C. Fu and S. Liu, *Ceramics International*, 2014, **40**, 5307-5311.

27 A. Reyhani, S. Z. Mortazavi, S. Mirershadi, A. N. Golikand and A. Z. Moshfegh, *International Journal of Hydrogen Energy*, 2012, **37**, 1919-1926.

28 K. Srinivas, S. M. Rao and P. V. Reddy, *Nanoscale*, 2011, **3**, 642-653.

29 J. P. Cheng, B. B. Wang, M. G. Zhao, F. Liu and X. B. Zhang, *Sensors and Actuators B: Chemical*, 2014, **190**, 78-85.

30 H. L. Ma, X. T. Hao, J. Ma, Y. G. Yang, J. Huang, D. H. Zhang, X. G. Xu, *Appl. Surf. Sci*., 2002, **191**, 313-318.

31 X. Cai, Y. Cai, Y. Liu, H. Li, F. Zhang and Y. Wang, *Journal of Physics and Chemistry of Solids*, 2013, **74**, 1196-1203.

32 B. Pandey, S. Ghosh, P. Srivastava, D. Kabiraj, T. Shripati and N. P. Lalla, *Physica E: Low-dimensional Systems and Nanostructures*, 2009, **41**, 1164-1168.

33 Y. Dong and J. Zheng, *J. Mol. Liq.*, 2014, **196**, 280-284.

34 Y. Jia, P. Y. Wu, Y. P. Jiang, Q. Y. Zhang, S. S. Zhou, F. Fang and D. Y. Peng, *New J. Chem.*, 2014, **38**, 1100-1105.

35 X. Qi, J. Xu, W. Zhong and Y. Du, *RSC Adv.*, 2015, **5**, 16010-16016.

36 M. Zong, Y. Huang, Y. Zhao, X. Sun, C. Qu, D. Luo and J. Zheng, *RSC Adv.*, 2013,

3, 23638-23648.

37 M. Zong, Y. Huang and N. Zhang, *Mater. Lett.*, 2015, **145**, 115-119.

38 G. Z. Wang, X. G. Peng, L. Yu, G. P. Wan, S. W. Lin and Y. Qin, *J. Mater. Chem. A*., 2015, **3**, 2734-2740.

39 B. Zhao, G. Shao, B. B. Fan, W. Y. Zhao, Y. Q. Chen and R. Zhang, *RSC Adv*., 2015, **5**, 9806-9814.

40 X. M. Zhang, G. B. Ji, W. Liu, B. Quan, X. H. Liang, C. M. Shang, Y. Cheng and Y. W. Du, *Nanoscale*, 2015, **7**, 12932-12942.

41 H. L. Lv, G. B. Ji, H. Q. Zhang and Y. W. Du, *RSC Adv*., 2015,**7**, 76836-76843.

42 S. He, G. S. Wang, C. Lu, J. Liu, B. Wen, H. Liu, L. Guo and M. S. Cao, *J. Mater. Chem. A*, 2013, **1**, 4685-4692.

43 H. Wu, L. Wang, S. Guo, Y. Wang and Z. Shen, *Mater. Chem. Phys.*, 2012, **133**, 965-970.

44 Y. L. Ren, H. Y. Wu, M. M. Lu, Y. J. Chen, C. L. Zhu, P. Gao, M. S. Cao, C. Y. Li and Q. Y. Ouyang, *ACS Appl. Mater. Interf.*, 2012, **4**, 6436-6442.

45 P. C. Watts, W. K. Hsu, A. Barnes and B. Chambers, *Adv. Mater.*, 2003, **15**, 600-603.